

TOI-132 b: A short-period planet in the Neptune desert transiting a $V = 11.3$ G-type star

Matías R. Díaz,^{1★} James S. Jenkins,¹ Davide Gandolfi,² Eric D. Lopez,³ Maritza G. Soto,⁴ Pía Cortés-Zuleta,¹ Zaira M. Berdinas,¹ Keivan G. Stassun,^{5,6} Karen A. Collins,⁷ José I. Vines,¹ Carl Ziegler,⁸ Malcom Fridlund,^{9,10} Eric L.N. Jensen,¹¹ Felipe Murgas,^{12,13} Alexandre Santerne,¹⁴ Paul A. Wilson,¹⁵ Massimiliano Esposito,¹⁶ Artie P. Hatzes,¹⁶ Marshall C. Johnson,¹⁷ Kristine W. F. Lam,¹⁸ John H. Livingston,¹⁹ Vincent Van Eylen,^{20,21} Norio Narita,^{12,22,23,24} Cesar Briceño,²⁵ Kevin I. Collins,²⁶ Szilard Csizmadia,²⁷ Michael Fausnaugh,²⁸ Tianjun Gan,²⁹ Iska Georgieva,⁹ Ana Glidden,^{28,30} Jon M. Jenkins,³¹ David W. Latham,⁷ Nicholas M. Law,³² Andrew W. Mann,³² Savita Mathur,¹² Ismael Mireles,²⁸ Robert Morris,^{31,33} Enric Pallé,^{12,13} Carina M. Persson,⁹ Stephen Rinehart,³ Mark E. Rose,³¹ Sara Seager,^{28,30,34} Jeffrey C. Smith,^{31,33} Thiam-Guan Tan,³⁵ Andrei Tokovinin,²⁵ Andrew Vanderburg,³⁶ Roland Vanderspek,²⁸ Daniel A. Yahalomi⁷

Authors' affiliations are shown at the end of the manuscript

Accepted XXX. Received YYY; in original form YYY

ABSTRACT

The Neptune desert is a feature seen in the radius-mass-period plane, whereby a notable dearth of short period, Neptune-like planets is found. Here we report the *TESS* discovery of a new short-period planet in the Neptune desert, orbiting the G-type dwarf TYC 8003-1117-1 (TOI-132). *TESS* photometry shows transit-like dips at the level of ~ 1400 ppm occurring every ~ 2.11 days. High-precision radial velocity follow-up with HARPS confirmed the planetary nature of the transit signal and provided a semi-amplitude radial velocity variation of ~ 11.5 m s⁻¹, which, when combined with the stellar mass of $0.97 \pm 0.06 M_{\odot}$, provides a planetary mass of $22.83^{+1.81}_{-1.80} M_{\oplus}$. Modeling the *TESS* high-quality light curve returns a planet radius of $3.43^{+0.13}_{-0.14} R_{\oplus}$, and therefore the planet bulk density is found to be $3.11^{+0.44}_{-0.450}$ g cm⁻³. Planet structure models suggest that the bulk of the planet mass is in the form of a rocky core, with an atmospheric mass fraction of $4.3^{+1.2}_{-2.3}\%$. TOI-132 b is a *TESS* Level 1 Science Requirement candidate, and therefore priority follow-up will allow the search for additional planets in the system, whilst helping to constrain low-mass planet formation and evolution models, particularly valuable for better understanding the Neptune desert.

1 INTRODUCTION

The *Kepler* space telescope (Borucki 2010) has allowed us to understand the population of small planets ($R_p < 4 R_{\oplus}$) in a real statistical sense for the first time. *Kepler* revealed that the majority of planets are the so-called super-Earths, with an occurrence rate of $\sim 6\%$ of Earth-size planets around Sun-like stars (Petigura et al. 2013). *Kepler* has also unveiled a bimodality in the radius distribution of such planets (Fulton et al. 2017; Van Eylen et al. 2018), which could be the result of photo-evaporation of the planetary atmosphere due to the intense stellar radiation (Lopez & Fortney 2013; Owen & Wu

2013; Jin et al. 2014; Chen & Rogers 2016). Furthermore, higher-mass planets in the Neptune regime are also more abundant than the large gas giant planets. It is important to note that the distinction between super-Earth and sub-Neptune is based only on the radius, where the first class is commonly defined as planets with $1 R_{\oplus} < R_p < 2 R_{\oplus}$ while the latter comprises planets with $2 R_{\oplus} < R_p < 4 R_{\oplus}$. From *Kepler* statistics, 25% of Sun-like stars in our galaxy are found to host at least one small planet ($R_p < 4 R_{\oplus}$) on a short period orbit ($P < 100$ d) (Batalha et al. 2013; Marcy et al. 2014).

Although Neptune-sized planets orbiting Sun-like stars are fairly abundant (e.g., Espinoza et al. 2016; Luque et al. 2019; Mayo et al. 2019; Palte et al. 2019), at short orbital periods they are very rare. A number of early studies indicated a lack of Neptune-sized planets with periods shorter than 2–4 days (Szabó & Kiss 2011; Benítez-Llambay et al. 2011; Beaugé & Nesvorný 2013; Helled et al. 2016), and the term “Neptune desert” was coined to explain this paucity. Mazeh et al. (2016) placed this dearth on a statistical footing, whilst providing robust boundaries for the region. Even though the dominant mechanism that produces this desert is currently unknown, models that invoke tidal disruption of a high-eccentricity migration planet, coupled with photoevaporation can explain the triangular shape of the gap described by Mazeh et al. (2016) (see also Lundkvist et al. 2016; Owen & Lai 2018).

The Neptune desert may be a region of parameter space with a paucity of such planets, but it is not completely empty. West et al. (2019) discovered the planet NGTS-4b as part of the Next Generation Transit Survey (Wheatley et al. 2018). Although the star is fairly faint ($V = 13.14$), making the constraints on the radius and mass difficult, the planet resides inside the boundaries of the desert, as defined by Mazeh et al. (2016). A more recent example was found using data from the Transiting Exoplanet Survey Satellite (*TESS*; Ricker et al. 2015): a planet orbiting the star HD 21966 residing in the edge of this region (Esposito et al. 2019). The primary goal of *TESS* is to discover 50 planets with radii $\leq 4 R_{\oplus}$ transiting stars brighter than $V \leq 12$, for which precise masses can be measured using high-precision Doppler spectroscopy, better constraining the planetary bulk density. In doing so, the mission is also providing unprecedented targets to follow-up to study the Neptune desert, particularly the discovery of the first ultra hot Neptune, LTT 9779 b (Jenkins et al. 2019). This planet resides on the edge of the Neptune desert, and since the star is bright ($V = 9.76$), detailed follow-up can be performed to shed light on the processes that sculpt the desert. However, more such examples are necessary in order to uncover the dominant process(es) at play.

Here we present the discovery of TOI-132 b, a $22.8-M_{\oplus}$ Neptune-sized planet discovered by *TESS* and confirmed using high-precision Doppler spectroscopy from the High Accuracy Radial velocity Planet Searcher (HARPS; Pepe et al. 2002).

2 PHOTOMETRY

2.1 *TESS* Photometry

TYC 8003-1117-1 (also known as TOI-132) was observed by *TESS* in Sector 1 on Camera 2 in short-cadence mode ($T_{\text{exp}} = 2$ minutes). The total time baseline of the observations is 27.87 days, spanning from July 25th to August 22nd 2018. TOI-132 b was identified as a potential transiting planet signature by the Science Processing Operations Center (SPOC) in the transit search run on Sector 1 (Jenkins 2002; Jenkins et al. 2010) and promoted to TOI status by the *TESS* Science Office based on the SPOC Data Validation (DV) reports (Twicken et al. 2018; Li et al. 2019).

The target was selected from the *TESS* alerts website¹, based on the magnitude of the star ($V = 11.2$ mag) and period of the candidate, since it presented a good opportunity to be confirmed relatively quickly with HARPS.

In addition, the DV report for TOI-132 b is very clean, and the planetary signature passed all of the diagnostic tests conducted by DV, including the odd/even depth test, the weak secondary test, the ghost diagnostic test, the difference image centroid shift test. We retrieved the photometry provided by the *TESS* SPOC pipeline (Jenkins et al. 2016), and accessed the data from the simple aperture photometry (SAP_FLUX) and the Presearch Data Conditioning simple aperture photometry (PDCSAP_FLUX, Smith et al. 2012; Stumpe et al. 2014), which contains systematics-corrected data using the algorithms previously used for *Kepler* (Jenkins 2017). The median-normalized SAP_FLUX photometry is shown in the top panel of Figure 1. Bottom panel shows the PDCSAP_FLUX photometry, divided by its median value and after applying a 4σ clipping rejection. This light curve is used throughout all the analyses in this paper. The gap in the middle of the time series occurred when the observations were stopped to allow for the data down-link. Finally, in order to avoid any bias in our analysis, we excluded the photometric measurements between (BJD - 2457000) 1347.5 and 1349.3 (gray shaded area) given that the spacecraft pointing jitter was higher than nominal, as described by Huang et al. (2018) and also noted in recent *TESS* discoveries (see, e.g., Espinoza et al. 2019a). A total of 11 transit events were considered for further analysis in the present work. Magnitudes and stellar parameters for TOI-132 are shown in Table 1 (see also Section 4).

2.2 Ground-based time-series photometry

We acquired ground-based time-series follow-up photometry of TOI-132 as part of the *TESS* Follow-up Observing Program (TFOP) to attempt to rule out nearby eclipsing binaries (NEBs) in all stars that could be blended in the *TESS* aperture as potential sources of the *TESS* detection. Furthermore, we attempt to *i*) detect the transit-like event on target to confirm the event depth and thus the *TESS* photometric deblending factor, *ii*) refine the *TESS* ephemeris, *iii*) provide additional epochs of transit center time measurements to supplement the transit timing variation (TTV) analysis, and *iv*) place constraints on transit depth differences across filter bands. We used the *TESS* Transit Finder, which is a customized version of the Tapir software package (Jensen 2013), to schedule our transit observations.

We observed TOI-132 continuously for 443 minutes on UTC 2018 September 09 in R_c band from the Perth Exoplanet Survey Telescope (PEST) near Perth, Australia. The 0.3-m telescope is equipped with a 1530×1020 pixels SBIG ST-8XME camera with an image scale of $1''.2 \text{ pixel}^{-1}$ resulting in a $31' \times 21'$ field of view. A custom pipeline was used to calibrate the images and extract the differential photometry using an aperture with radius $8''.2$. The images have typical stellar point spread functions (PSFs) with a full width at half maximum (FWHM) of $\sim 4''$. The data rule out NEBs

¹ <https://tev.mit.edu/data/>

Table 1. Stellar parameters for TOI-132.

Parameter	Value	Source
<i>TESS</i> Names	TIC89020549 (TOI-132.01)	
RA (hh:mm:ss)	22:33:35.8683	<i>Gaia</i>
Dec (dd:mm:ss)	-43:26:11.9167	<i>Gaia</i>
μ RA (mas yr ⁻¹)	35.553 ± 0.043	<i>Gaia</i>
μ (mas yr ⁻¹)	-53.055 ± 0.054	<i>Gaia</i>
Parallax (mas)	6.08 ± 0.04	<i>Gaia</i> *
Distance (pc)	164.47 ± 27.32	<i>Gaia</i>
SpT	G8V	This work
Photometry		
<i>B</i>	12.07 ± 0.17	Tycho-2
<i>V</i>	11.29 ± 0.07	Tycho-2
<i>g</i>	11.85 ± 0.02	APASS
<i>r</i>	11.24 ± 0.01	APASS
<i>i</i>	11.08 ± 0.02	APASS
<i>TESS</i>	10.80 ± 0.02	Stassun et al. (2018b)
<i>Gaia</i>	11.2935 ± 0.0003	<i>Gaia</i>
<i>J</i>	10.14 ± 0.02	2MASS
<i>H</i>	9.76 ± 0.02	2MASS
<i>K_s</i>	9.65 ± 0.02	2MASS
<i>W₁</i>	9.61 ± 0.02	WISE
<i>W₂</i>	9.69 ± 0.02	WISE
<i>W₃</i>	9.60 ± 0.04	WISE
<i>W₄</i>	8.72 ± 0.42	WISE
Derived Parameters		
<i>T_{eff}</i> (K)	5397 ± 46	This work
log <i>g</i> (cm s ⁻²)	4.48 ± 0.23	This work
[Fe/H] (dex)	0.16 ± 0.10	This work
<i>L</i> (<i>L_⊙</i>)	0.60 ± 0.05	This work
<i>R</i> (<i>R_⊙</i>)	0.90 ± 0.02	This work
<i>M</i> (<i>M_⊙</i>)	0.97 ± 0.06	This work
<i>v sin(i)</i> (km s ⁻¹)	3.00 ± 0.30	This work
<i>v_{mac}</i> (km s ⁻¹)	1.74 ± 0.20	This work
ρ_* (g cm ⁻³)	1.89 ± 0.15	This work
log <i>RHK</i> (dex)	-5.02 ± 0.13	This work
Age (Gyr)	6.34 ^{+0.42} _{-2.35}	This work
(U,V,W) (km s ⁻¹)	18.4 ± 0.2, -32.6 ± 0.4, 16.5 ± 0.4	This work

*Correction of +82 μ as from Stassun & Torres (2018) applied to the *Gaia* value.

in stars within 2.5 of the target star that are fainter by as much as 6.4 magnitudes in *R_c* band.

We also observed full predicted transit durations of TOI-132 continuously in z-short band on UTC 2018 November 14, UTC 2019 June 19, and UTC 2019 July 06 from the Las Cumbres Observatory (LCO) 1.0 m telescopes (Brown et al. 2013) at Cerro Tololo Inter-American Observatory for 277, 335, and 283 minutes, respectively. Another full transit was observed continuously for 232 minutes in B-band on UTC 2019 August 02 from an LCO 1.0 m telescope at Siding Spring Observatory. The 4096 × 4096 LCO SINISTRO cameras have an image scale of 0.389 pixel⁻¹ resulting in a 26' × 26' field of view. The images were calibrated by the standard LCO BANZAI pipeline (McCully et al. 2018) and the photometric data were extracted using the AstroImageJ (AIJ) software package (Collins et al. 2017).

The November data rule out NEBs in all stars within 2.5 of the target star that are fainter by as much as 8.7 magnitudes in z-short band, which includes all known *Gaia* DR2 stars that are blended in the *TESS* aperture. The

June observation confirmed a ~1400 ppm deep ingress on target arriving ~80 minutes late relative to the original TOI ephemeris. The follow-up ephemeris was adjusted to account for the 80 minute offset. The July observation confirmed an on-time arrival of a ~1400 ppm deep full transit relative to the adjusted ephemeris, indicating that the transit timing is consistent with a linear ephemeris. The images have stellar PSF FWHMs of ~2.0", and the transit signal is reliably detected on target using a follow-up aperture with radius as small as 1.5". Therefore, the aperture is negligibly contaminated by the nearest *Gaia* neighbor 10.5" south. Systematic effects start to dominate the light curve for smaller apertures. The August B-band observation confirmed an on-time arrival of a ~1400 ppm deep full transit, indicating that the transit-like event does not show a filter dependent depth in B and z-short bands, which photometrically strengthens the case for a transiting exoplanet orbiting around TOI-132.

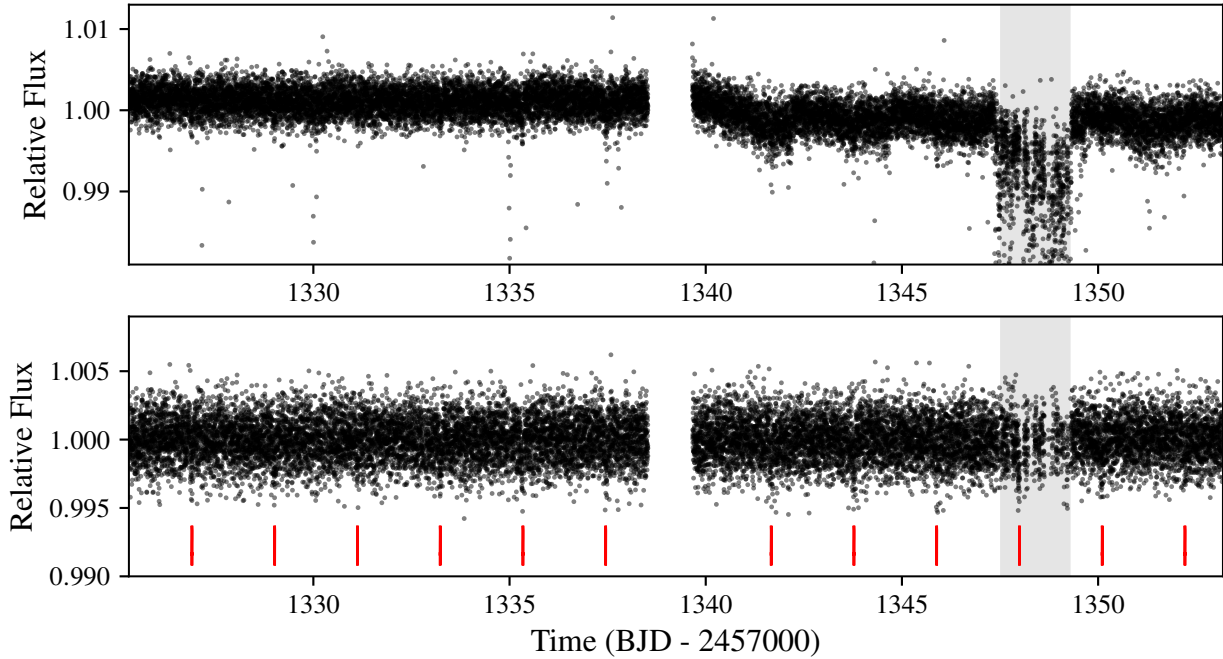


Figure 1. *TESS* light curve for TOI-132. Top panel shows the Simple Aperture Photometry (SAP_FLUX). Bottom panel shows the systematic-corrected PDCSAP_FLUX photometry after normalizing by the median and rejecting 4σ values. Red vertical lines show the position of the 12 transits identified in the *TESS* alert from Sector 1.

3 HARPS SPECTROSCOPIC FOLLOW-UP

TOI-132 was observed using HARPS (Pepe et al. 2002) spectrograph mounted at the 3.6-m ESO telescope at La Silla observatory, during seven consecutive nights between April 2 and 9 2019, as part of the observing program 0103.C-0442. The exposure time was set to 1200-1800 sec, which allowed us to achieve a mean signal-to-noise (S/N) ratio of ~ 35 per pixel at 5500 \AA in the extracted spectra. Upon examination of the radial velocities and after performing a 1-planet model fit to the *TESS* period, we found it necessary to acquire more observations to improve the phase coverage. Therefore, 13 additional radial velocities were taken in two runs between May and July 2019, as part of the observing program 1102.C-0923, covering the initial gaps in the orbital phase from the observations in April. We set the exposure time to 1800-2100 sec, leading to a mean S/N ratio of ~ 40 .

We reduced the spectra using the HARPS online data reduction software (DRS) (Bouchy et al. 2001). The data products include the extracted spectra, both in *echelle* and order-merged spectra, the cross-correlation functions² (CCF, Baranne et al. 1996; Pepe et al. 2002) and a measurement of the full-width at half maximum (FWHM) of the CCF profile, and the bisector inverse slope (BIS, Queloz et al. 2001).

We extracted the radial velocity measurements using the HARPS-TERRA package (Anglada-Escudé et al. 2012). The algorithm creates a high signal-to-noise template by combining all the observed spectra, based on their signal-to-noise ratio, and then it recomputes the radial velocity of

a given observation by matching each individual spectrum with the template. One advantage for choosing HARPS-TERRA is that RVs are computed for every echelle order so it is relatively easy to find the orders with most of the RV information, discarding contaminated or low S/N orders. In this case, we chose the first 22 orders as they produced lowest errors and smallest RMS in the RVs. The software does not compute the BIS nor FWHM of the CCF, which are taken directly from the DRS using a G2 mask. TERRA does compute activity indicators in the form of S-indices directly from each observed spectrum. The S-index is measured from the cores of the Calcium II H & K lines ($\lambda_H = 3933.664 \text{ \AA}$, $\lambda_K = 3968.470 \text{ \AA}$) and compared with the flux on adjacent chunks in the continuum, following the prescription from Lovis et al. (2011) and it is calibrated to the Mt. Wilson system (S_{MW}), serving as a direct proxy to monitor the chromospheric activity of the star. Uncertainties in BIS are taken as twice the internal RV errors and the FWHM error are 2.35 times the RV uncertainties (see Zechmeister et al. 2013; Santerne et al. 2015). The results are shown in Table 2.

Figure 2 shows the correlations between radial velocities and activity indicators, BIS, FWHM CCF and S_{MW} , from left to right, respectively. No correlations are seen between the radial velocities and the activity indicators. However, we note one outlier point in the FWHM and S-index, which was related with an observation acquired under poor weather conditions at the beginning of the observing run in April 2019.

² Obtained using a G2 numerical mask.

We computed the Generalized Lomb-Scargle peri-

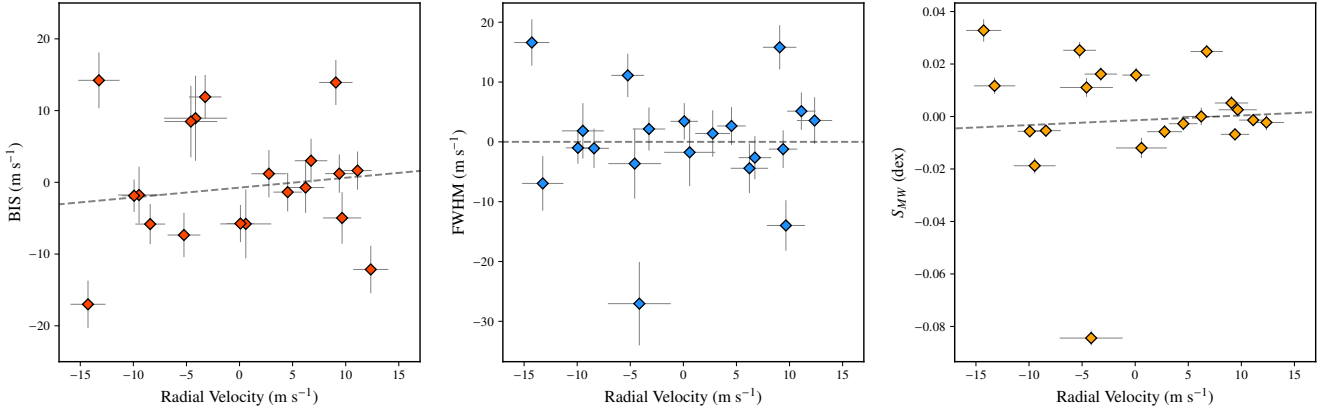


Figure 2. Left to right: correlations between BIS, cross-correlation function FWHM, S-index and radial velocities after subtraction of their mean, respectively. The first two are obtained from DRS and the latter is derived from the HARPS spectra using the HARPS-TERRA algorithm. On each plot, the dashed line represents a linear fit between the activity index and radial velocity. All three plots shows no strong evidence for correlation, although outliers are seen in the FWHM and S_{MW} .

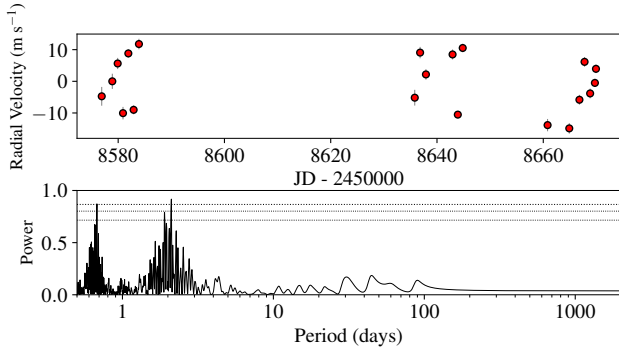


Figure 3. Top: Time series showing the radial velocities from the HARPS follow-up observations. Bottom: Generalized Lomb-Scargle periodogram of the radial velocities. Horizontal lines, from bottom to top, represent the 10, 1 and 0.1% significance levels estimated via 5000 bootstrap samples.

odogram³ (GLS; Zechmeister & Kürster 2009) of the HARPS Doppler measurements and activity indicators. As shown in Figure 3, the GLS periodogram of the HARPS RVs shows a significant peak at the orbital period of the transiting planet (2.11 d) with a false-alarm probability $FAP < 0.1\%$. We note that the secondary peak with $FAP < 1\%$ is the 1-day alias of the orbital period. The periodograms of the HARPS activity indicators show neither a significant peak matching the one found in the RVs, nor any other significant peaks (Figure 4).

4 STELLAR PARAMETERS

We first estimated the stellar parameters by combining the HARPS spectra into a high-S/N ratio spectrum and fed that into the SPECIES code (Soto & Jenkins 2018). For a more

³ `astropy.timeseries.LombScargle()`, <https://docs.astropy.org/en/stable/timeseries/lombscargle.html>.

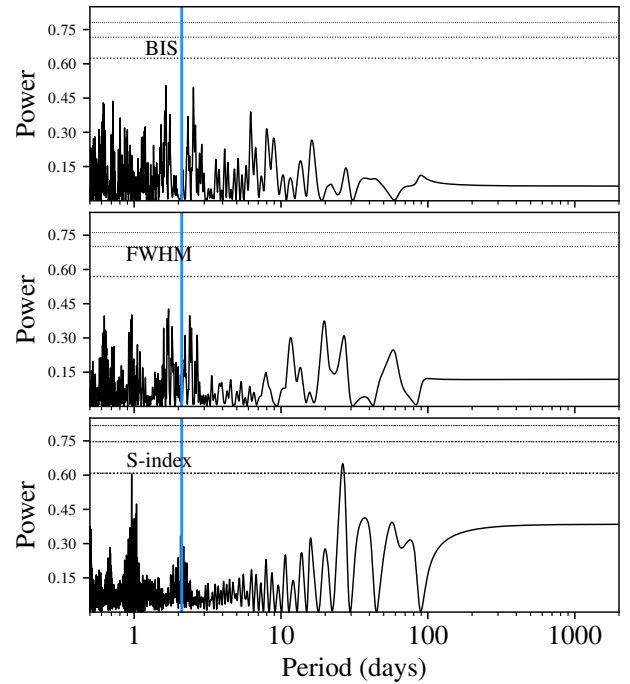


Figure 4. Top to bottom: Generalized Lomb-Scargle periodogram for the activity indices obtained with HARPS: BIS, FWHM and S-index, respectively. Horizontal lines, from bottom to top, represent the 10, 1 and 0.1% significance levels estimated via 5000 bootstrap samples. Vertical line on each plot marks the position of the 2.11-day planet candidate signal present in the radial velocity.

detailed explanation and outputs from this code, the reader is referred to Díaz et al. (2018) and Soto & Jenkins (2018).

We also analyzed the combined HARPS spectrum using both Spectroscopy Made Easy (SME, version 5.22; Valenti & Piskunov 1996a,b; Piskunov & Valenti 2017), and the empirical package SpecMatch-Emp (Yee et al. 2017). We followed the same procedures outlined in, e.g., Fridlund et al. (2017),

Table 2. HARPS Radial Velocities and spectral activity indices for TOI-132

BJD	RV	σ RV	S_{MW}	σS_{MW}	FWHM	σ FWHM	BIS	σ BIS
(- 2450000)	(m s ⁻¹)	(m s ⁻¹)	(dex)	(dex)	(km s ⁻¹)	(m s ⁻¹)	(m s ⁻¹)	(m s ⁻¹)
8576.90725	-4.737	2.967	0.056	0.003	6.885	16.180	2.967	5.933
8578.89655	0.000	2.398	0.128	0.004	6.911	16.240	2.398	4.797
8579.90764	5.631	1.765	0.140	0.003	6.908	16.234	1.765	3.531
8580.90988	-10.056	1.972	0.121	0.003	6.914	16.248	1.972	3.943
8581.91433	8.808	1.338	0.133	0.002	6.911	16.241	1.338	2.675
8582.91045	-9.005	1.402	0.135	0.002	6.911	16.241	1.402	2.803
8583.90870	11.771	1.656	0.138	0.003	6.916	16.252	1.656	3.312
8635.81477	-5.174	2.488	0.151	0.004	6.909	16.235	2.488	4.977
8636.82174	9.069	1.800	0.143	0.003	6.898	16.211	1.800	3.599
8637.91868	2.175	1.649	0.134	0.003	6.914	16.247	1.649	3.297
8642.93057	8.481	1.571	0.145	0.003	6.928	16.281	1.571	3.142
8643.91730	-10.522	1.129	0.134	0.002	6.911	16.242	1.129	2.257
8644.84072	10.526	1.331	0.139	0.002	6.917	16.256	1.331	2.662
8660.81222	-13.834	1.945	0.152	0.003	6.905	16.228	1.945	3.891
8664.89377	-14.864	1.652	0.173	0.004	6.929	16.283	1.652	3.305
8666.80357	-5.826	1.542	0.165	0.003	6.923	16.270	1.542	3.084
8667.76863	6.145	1.530	0.165	0.003	6.910	16.238	1.530	3.061
8668.82036	-3.829	1.534	0.156	0.003	6.914	16.249	1.534	3.067
8669.71698	-0.505	1.294	0.156	0.003	6.916	16.252	1.294	2.588
8669.91776	3.943	1.344	0.137	0.003	6.915	16.250	1.344	2.687

Table 3. Below are the priors used for TOI-132 for the *final* joint analysis fit using *juliet*. As a reminder, $p = R_p/R_*$ and $b = (a/R_*)\cos(i_p)$, where R_p is the planetary radius, R_* the stellar radius, a the semi-major axis of the orbit and i_p the inclination of the planetary orbit with respect to the plane of the sky. e and ω are the eccentricity and argument of periastron of the orbits. The prior labels of \mathcal{N} , $\tilde{\mathcal{N}}$, \mathcal{U} , and \mathcal{J} represent normal, truncated normal, uniform, and Jeffreys distributions. See text for explanations about other parameters.

Parameter name	Prior	Units	Description
Parameters for planet b			
P_b	$\mathcal{N}(2.10937, 0.001)$	days	Period.
$T_{0,b} - 2458000$	$\mathcal{N}(337.451, 10)$	days	Time of transit-center.
$r_{1,b}$	$\mathcal{U}(0, 1)$	—	Parametrization for p and b^1 .
$r_{2,b}$	$\mathcal{U}(0, 1)$	—	Parametrization for p and b^1 .
a_b	$\mathcal{U}(4.5, 7.0)$	—	scaled semi-major axis.
K_b	$\mathcal{N}(12.1, 2.0)$	m s ⁻¹	Radial-velocity semi-amplitude.
e_b	$\tilde{\mathcal{N}}(0, 0.1, 0, 0.25)$	—	eccentricity.
ω_b	$\mathcal{U}(0, 359.)$	degrees	argument of periastron.
Parameters for TESS			
D_{TESS}	1.0 (Fixed)	—	Dilution factor for <i>TESS</i> .
M_{TESS}	$\mathcal{N}(0, 1)$	ppm	Relative flux offset for <i>TESS</i> .
$\sigma_{w,\text{TESS}}$	$\mathcal{J}(0.1, 100)$	ppm	Extra jitter term for <i>TESS</i> lightcurve.
$q_{1,\text{TESS}}$	$\mathcal{U}(0, 1)$	—	Quadratic limb-darkening parameter.
$q_{2,\text{TESS}}$	$\mathcal{U}(0, 1)$	—	Quadratic limb-darkening parameter.
Parameters for LCO			
D_{LCO}	1.0 (Fixed)	—	Dilution factor for LCO.
M_{LCO}	$\mathcal{N}(0, 1)$	ppm	Relative flux offset for LCO.
$\sigma_{w,\text{LCO}}$	$\mathcal{J}(0.1, 100)$	ppm	Extra jitter term for LCO lightcurve.
$q_{1,\text{LCO}}$	$\mathcal{U}(0, 1)$	—	Quadratic limb-darkening parameter.
$q_{2,\text{LCO}}$	$\mathcal{U}(0, 1)$	—	Quadratic limb-darkening parameter.
Parameters for HARPS			
μ_{HARPS}	$\mathcal{N}(-0.6, 1.)$	m s ⁻¹	Radial velocity zero-point (offset).
$\sigma_{w,\text{HARPS}}$	$\mathcal{J}(0.1, 10)$	m s ⁻¹	Extra jitter term for HARPS radial velocity.

¹We used the transformations outlined in Espinoza (2018) and also set $p_l=0.03$ and $p_u=0.05$ in the *juliet* call.

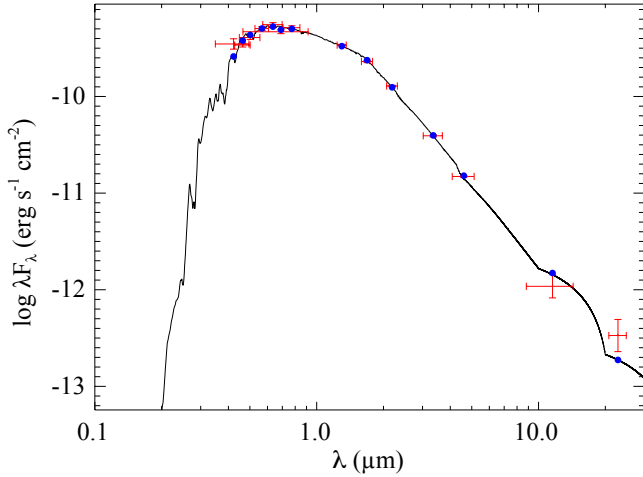


Figure 5. Spectral energy distribution of TOI-132. The blue points are the predicted integrated fluxes and the red symbols are the observed values at the corresponding passbands, where the horizontal bars represent the effective width of the passband and the vertical errors represent the 1σ uncertainties. The best-fit Kurucz atmospheric model for TOI-132 is shown by the black solid line.

Persson et al. (2018, 2019), Gandolfi et al. (2019). The two methods provide consistent results within $1\text{--}2\sigma$, which are also in agreement with those obtained with SPECIES. In particular, the age of the star was determined by isochrone fitting according to the method described in SPECIES. We note that, while there is no reason to prefer one set of spectroscopic parameter estimates over the others, we adopted the results derived with SPECIES for the subsequent analyses presented in this work.

We performed an analysis of the broadband spectral energy distribution (SED) of the star together with the *Gaia* DR2 parallaxes (adjusted by $+0.08$ mas to account for the systematic offset reported by Stassun & Torres 2018), in order to determine an empirical measurement of the stellar radius, following the procedures described in Stassun & Torres (2016) and Stassun et al. (2017, 2018a). We retrieved the NUV flux from *GALEX*, the $B_T V_T$ magnitudes from *Tycho-2*, the $B_V g r i$ magnitudes from APASS, the JHK_S magnitudes from 2MASS, the W1–W4 magnitudes from *WISE*, and the G magnitude from *Gaia*. Together, the available photometry spans the full stellar SED over the wavelength range $0.2\text{--}22\text{ }\mu\text{m}$ (see Figure 5).

We performed a fit using Kurucz stellar atmosphere models, with the effective temperature (T_{eff}) and metallicity ($[\text{Fe}/\text{H}]$) and surface gravity ($\log g$) adopted from the spectroscopic analysis of SPECIES. The only free parameter is the extinction (A_V), which we restricted to the maximum line-of-sight value from the dust maps of Schlegel et al. (1998). The resulting fit shown in Figure 5, gives a reduced χ^2 of 2.4 and best-fit $A_V = 0.03 \pm 0.01$. Integrating the (unreddened) model SED, it gives the bolometric flux at Earth, $F_{\text{bol}} = 7.492 \pm 0.087 \times 10^{-10} \text{ erg s}^{-1} \text{ cm}^{-2}$. Taking the F_{bol} and T_{eff} together with the *Gaia* DR2 parallax, gives the stellar radius, $R_\star = 0.90 \pm 0.02 R_\odot$. Finally, we can use the empirical relations of Torres et al. (2010) and a 6% error from the empirical relation itself to estimate the stellar mass,

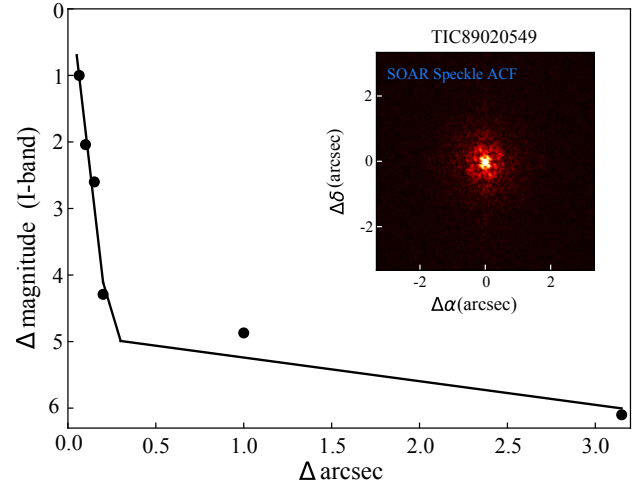


Figure 6. Speckle imaging for TOI-132 obtained with SOAR. Inset on the top right corner shows a preview of the ACF.

$M_\star = 0.97 \pm 0.06 M_\odot$; this, in turn, together with the stellar radius provides an empirical estimate of the mean stellar density $\rho_\star = 1.89 \pm 0.15 \text{ g cm}^{-3}$. We note the small errorbars on both stellar mass and radius come directly from propagation of uncertainties in T_{eff} , F_{bol} , and parallax. In this case, the fractional errors are of order $\sim 1\%$, $\sim 1\%$ and $\sim 0.5\%$, respectively. Then, the uncertainty in stellar radius is dominated by the T_{eff} error, in this case that implies an error of $\sim 2\%$ (see Table 1).

5 SPECKLE IMAGING

The relatively large 21-arcsec pixels of *TESS* can result in contamination from companion stars or nearby sources. The additional light from these can dilute the planetary transit, resulting in an underestimated planet radius. We searched for nearby sources with speckle imaging with HRCam on the 4.1-m Southern Astrophysical Research (SOAR) telescope (Tokovinin et al. 2018) on 2018 September 25 UT. From these observations, a potential companion star was detected at low-significance. The purported star was located near the first diffraction ring of the primary star, at 0.079 arcsec (and a projected distance of ~ 12 AU), a similar position as optical ghosts which can occasionally appear in the speckle imaging during periods of low wind. This triggered a warning as the flux contamination due to the companion ($\Delta m \sim 2.6$ mag) would have not been negligible for the spectroscopic observations given that the diameter of the fibers on HARPS is ~ 1 arcsec, meaning that the suspected companion was inside the aperture of the fiber. Upon visual inspection of the CCF and the individual spectra, we could not see evidence for such a contamination. The system was observed again on 2019 May 18 UT in excellent conditions, and the possible companion star was not detected. The $5\text{-}\sigma$ detection sensitivity and auto-correlation function of the later observation are shown in Figure 6.

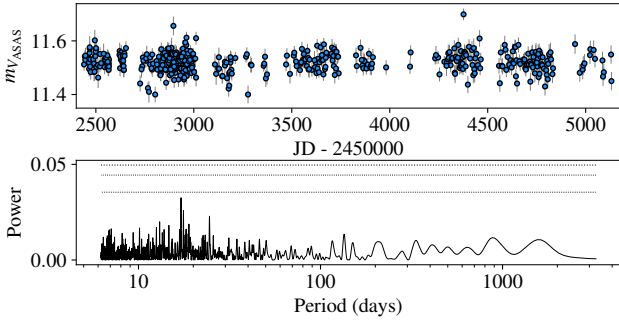


Figure 7. ASAS V-band photometry for TOI-132 to search for additional sources of periodicity in the star. The bottom plot shows the Generalized Lomb-Scargle periodogram of the time series. Horizontal lines, from bottom to top, represent the 10, 1 and 0.1% significance levels estimated via 5000 bootstrap samples.

6 ASAS PHOTOMETRY

We analyzed photometry from the All-Sky Automated Survey (ASAS, [Pojmanski 1997](#)) to search for stellar rotational periods. There are 694 available photometric measurements spanning 8.9 years, from November 2000 to December 2009. The selection of the best aperture was made choosing the time series with the lowest Median Absolute Deviation (MAD). We discarded 129 points that were flagged as bad datapoints, including only 565 measurements with either “A” or “B” quality. Figure 7 shows the photometric time series after removing outliers and bad data and the GLS.

From the power spectrum in the periodogram the highest power is found to be at 17.138 days. We estimated the 10, 1 and 0.1% significance level by running 5000 bootstrap samplings using the implementation available in the Python module `astrostats.false_alarm_probability()`⁴. Although the highest peak in the GLS periodogram is noticeable and unique, its significance is below the 10% level, as seen from the bottom panel in the figure.

7 JOINT ANALYSIS

We modeled the radial velocities and the photometry using the `juliet`⁵ package ([Espinoza et al. 2019b](#)). Table 3 shows the priors used in the analysis. We set up the initial priors for the period of the candidate and the time of transit (T_0) using the reported values in the *TESS* DV report document for TOI-132.

Preliminary analysis was done by making use of `Systemic Console v2` ([Meschiari et al. 2009](#)). We analyzed the radial velocities only to get an initial rough estimate of both instrumental and orbital parameters of the system such as the velocity semi-amplitude, eccentricity and minimum mass of the planet. The period and transit time were constrained using the updated values provided by *TESS*. Initial results for a 1-planet model with eccentricity fixed at zero, yields

an $\text{RMS} \sim 2.7 \text{ m s}^{-1}$. Letting eccentricity and argument of periastron as free parameters the best-fit model RMS goes down to $\sim 2.5 \text{ m s}^{-1}$ and $e \sim 0.17$. With this information from the `Systemic` analysis we set up the priors on two runs with `juliet`. This package has been proven to be an excellent tool for analyzing both photometry and radial velocities using a joint model (see e.g., [Brahm et al. 2019](#); [Espinoza et al. 2019a](#); [Kossakowski et al. 2019](#)). In short, the code uses `batman` ([Kreidberg 2015](#)) to model the transit data and `radvel` ([Fulton et al. 2018](#)) to model the radial velocities, and in order to estimate the Bayesian log-evidence, $\ln Z$, for model comparison we used the option of the Dynamic Nested Sampling algorithm that the `dynesty` ([Speagle & Barbary 2018](#); [Speagle 2019](#)) package provides. We note that, while `juliet` has the option to include Gaussian Processes to model the lightcurve, radial velocities or both, we did not set this option as there was no evidence of additional variability in the PDCSAP_FLUX-corrected lightcurve (see Figure 1). We also used the parametrization described in [Espinoza \(2018\)](#) that allows an efficient way to sample the impact parameter, b , and the planet-to-star radius ratio, p , where only values that are physically plausible in the (p, b) plane are sampled via the r_2 and r_2 coefficients ([Espinoza 2018](#)). For the limb-darkening coefficients, we use the parametrization of [Kipping \(2013\)](#) for two parameter laws. All the prior information is listed in Table 3.

We set up two different runs, first by fixing eccentricity to zero, and another treating it (along with ω) as free parameter. Comparing the evidences from the circular ($\ln Z = 89705.63$) and eccentric model ($\ln Z = 89709.05$) we obtain $\Delta \ln Z = 3.41$ which suggests moderate evidence the latter is preferred over the circular one according to the model selections criteria and thresholds described in [Espinoza et al. \(2019b\)](#). The joint model results are shown in Figure 8.

As a sanity check, we also performed an independent joint analysis using the Python/FORTRAN software suite `pyaneti` ([Barragán et al. 2019a](#)). Results are consistent with those obtained with `juliet` well within the nominal error bars.

Using the luminosity of the host star, we could retrieve the incident flux on TOI-132 b by using the planet radius and semi-major axis from our joint model. We estimated that the insolation of TOI-132 b is $S_p = 860 S_\oplus$.

In order to estimate the average equilibrium temperature of the planet, considering the physical properties of TOI-132 b we assumed a Bond albedo of $A_B = 0.31$, that corresponds to the value accepted for Neptune. Then

$$T_{\text{eq}} = T_* \sqrt{\frac{R_*}{2a}} (1 - A_B)^{\frac{1}{4}} \quad (1)$$

yields an equilibrium temperature of $T_{\text{eq}} = 1384^{+53}_{-75} \text{ K}$ for the planet.

8 TTV ANALYSIS

In order to search for possible Transit Timing Variations in TOI-132 b, we computed the individual transit time of each light curve using the EXOFASTv2 code ([Eastman et al. 2013](#); [Eastman 2017](#)). EXOFASTv2 uses the Differential Evolution Markov chain Monte Carlo method (DE-MCMC) to derive

³ MAD = median($|X_i - \bar{X}|$)/0.6745

⁴ <https://docs.astrostats.org/en/stable/timeseries/lombscargle.html>

⁵ <https://github.com/nespinoza/juliet>

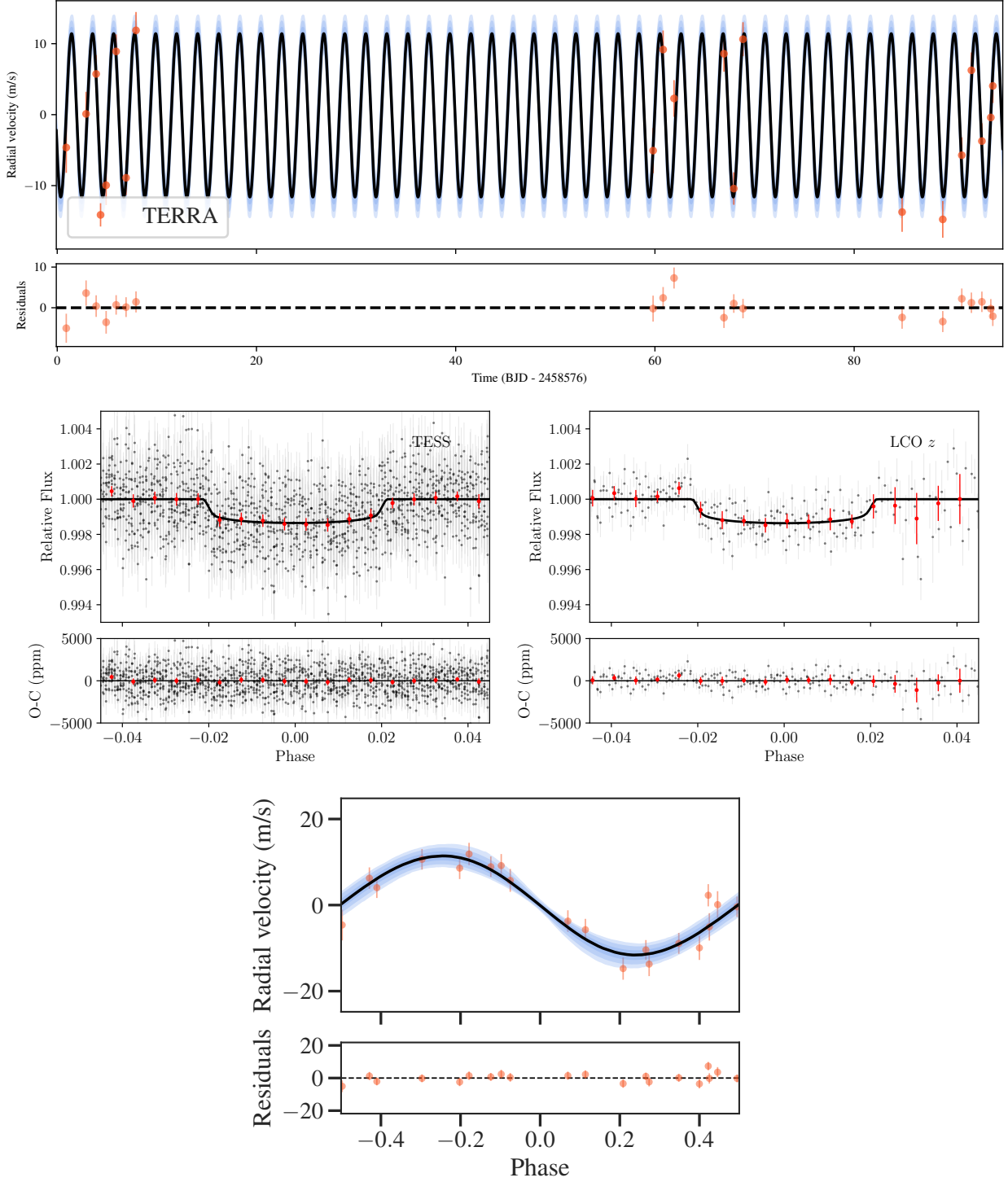


Figure 8. Results from the joint fit for the 1-planet model. *Top panel:* HARPS-TERRA radial velocities and best-fit Keplerian model (solid curve) the bands around it show 68%, 95% and 99% posterior credibility bands. *Mid panels:* *TESS* photometry (left) and LCO *z*-short photometry (right) phase-folded to the 2.109 d period of TOI-132 b along with best-fit transit model from the joint fit. Red points show the binned photometry in phase bins of 0.005. *Bottom panel:* phase-folded RVs from HARPS. The black line shows the model. Credibility bands are shown in the same way as in top panel. The error bars of both photometry and RV data include their corresponding jitter.

Table 4. Planetary Properties for TOI-132 b

Property	Value
Fitted Parameters	
P (days)	$2.1097008^{+0.000012}_{-0.000011}$
T_0 (BJD - 2450000)	$8343.77954^{+0.000093}_{-0.000092}$
a/R_*	$6.325^{+0.440}_{-0.657}$
b	$0.583^{+0.107}_{-0.149}$
K ($m s^{-1}$)	$11.58^{+0.78}_{-0.77}$
i_p (deg)	$84.63^{+1.58}_{-5.63}$
e	$0.087^{+0.054}_{-0.057}$
ω (deg)	$125.47^{+109.89}_{-53.77}$
Derived Parameters	
M_p (M_\oplus)	$22.83^{+1.81}_{-1.80}$
R_p (R_\oplus)	$3.43^{+0.13}_{-0.14}$
a (AU)	$0.026^{+0.002}_{-0.003}$
ρ_p ($g cm^{-3}$)	$3.11^{+0.44}_{-0.45}$
T_{eq} (K)	1384^{+53}_{-75}
Instrumental Parameters	
M_{TESS} (ppm)	$-0.000068^{+0.000013}_{-0.000012}$
$\sigma_{w,TESS}$ (ppm)	$8.01^{+23.29}_{-5.83}$
$q1,TESS$	$0.296^{+0.321}_{-0.188}$
$q2,TESS$	$0.345^{+0.342}_{-0.221}$
M_{LCO} (ppm)	$-0.000057^{+0.000059}_{-0.000058}$
$\sigma_{w,LCO}$ (ppm)	$461.28^{+73.22}_{-73.90}$
$q1,LCO$	$0.374^{+0.304}_{-0.230}$
$q2,LCO$	$0.321^{+0.323}_{-0.208}$
μ_{HARPS} ($m s^{-1}$)	$-0.11^{+0.51}_{-0.52}$
$\sigma_{w,HARPS}$ ($m s^{-1}$)	$1.99^{+0.71}_{-0.57}$

the values and their uncertainties for the stellar, orbital and physical parameters of the system.

So as to obtain the transit time of each light curve, we fixed the stellar and orbital parameters to the values obtained from the global fit performed by *juliet*, except for the transit time and their baseline flux. If a planet follows strictly a Keplerian orbit, the transit time of a given epoch $T_c(E)$ is a linear function of the orbital period P :

$$T_c(E) = T_c(0) + P \times E \quad (2)$$

Where $T_c(0)$ is a reference transit time and E is the number of epochs since $T_c(0)$. The best-fit values for equation 2 from *juliet* are shown in Table 4 along with the planetary parameters fixed to compute the individual transit time.

Considering the theoretical and the observed transit times of the light curves, we obtained the TTV values for TOI-132 b presented in Figure 9. Even though the larger variation is about 22 minutes, we found no evidence of a clear periodic variation in the transit time. This outlier is probably induced by a gap in the light curve of epoch 5. The RMS variation from the linear ephemeris is $\sigma = 8.03$ min, however, the reduced chi-squared for this model is $\chi^2_{red} = 1.37$. This is an indicator that the transit times, considering their errors, fit well with the proposed linear ephemeris.

The lack of an additional RV signal as well as no evidence of a TTV signal for our given time-span of our transit

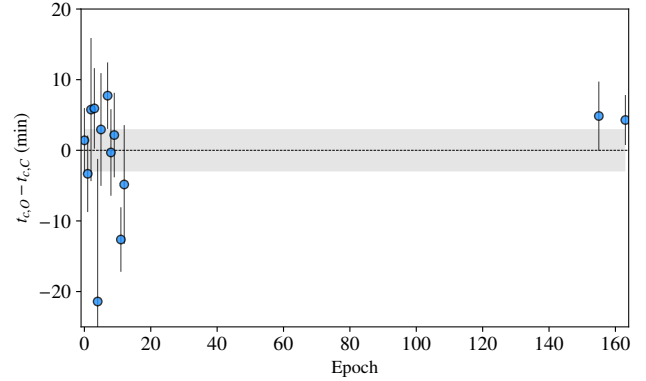


Figure 9. Observed minus computed mid-transit times of TOI-132 b. The residuals (TTV) of the transit times are shown considering the proposed linear ephemeris. The dashed line corresponds to zero variation and the grey area is the propagation of 1σ uncertainties, considering the optimal transit time from EXOFASTv2, and the period from *juliet*. The epoch 0 is the first transit observed by *TESS* and it is also the corresponding epoch of the optimal transit time. The TTV values shown in this plot fit accordingly with the proposed linear ephemeris ($\chi^2_{red} = 1.37$)

data, suggest that there is no other close-in companion of TOI-132 b. Nevertheless, further ground-based follow-up will be required to unveil the possible existence of companions in TOI-132.

9 DISCUSSION AND CONCLUSIONS

By combining *TESS* space-based photometry with HARPS high-precision radial-velocity measurements, along with additional high-sensitivity ground-based photometric observations, we were able to confirm a short period, hot Neptune-like planet orbiting the nearby metal-rich G8 V star TOI-132. The planet was found to have an orbital period of only 2.1 days, a radius of $3.43^{+0.13}_{-0.14} R_\oplus$, and mass of $22.83^{+1.81}_{-1.80} M_\oplus$, implying a density and equilibrium temperature of $3.108^{+0.44}_{-0.45} g cm^{-3}$ 1384^{+53}_{-75} K, respectively.

In Fig. 10 we can see that TOI-132 b is located in an underpopulated region of the mass-radius diagram. Of the relatively small number of known Neptune-like planets with well constrained properties, TOI-132 b stands out as bridging the gap between 100% water worlds and more typical Neptunes that have atmospheric mass fractions of $\sim 10\%$. The planet likely more closely resembles NGTS-4 b (West et al. 2019), which is shown in the figure despite the relatively high uncertainties measured for the planetary parameters, or TOI-824 b (Burt et al. 2019, private communication). These three planets appear to have similar masses and radii, giving rise to similar densities and bulk compositions, which might indicate they share similar formation histories.

Moreover, it is interesting to mention the planet K2-100 b from the *K2* mission Mann et al. (2017). Recently characterized by (Barragán et al. 2019b), the planet consists of a young, inflated Neptune on a short period around a G-type star. TOI-132 b falls within the evolutionary range of K2-100 b after 5 Gyr. This may indicate in the past TOI-132 b could have shared similar characteristics to that of

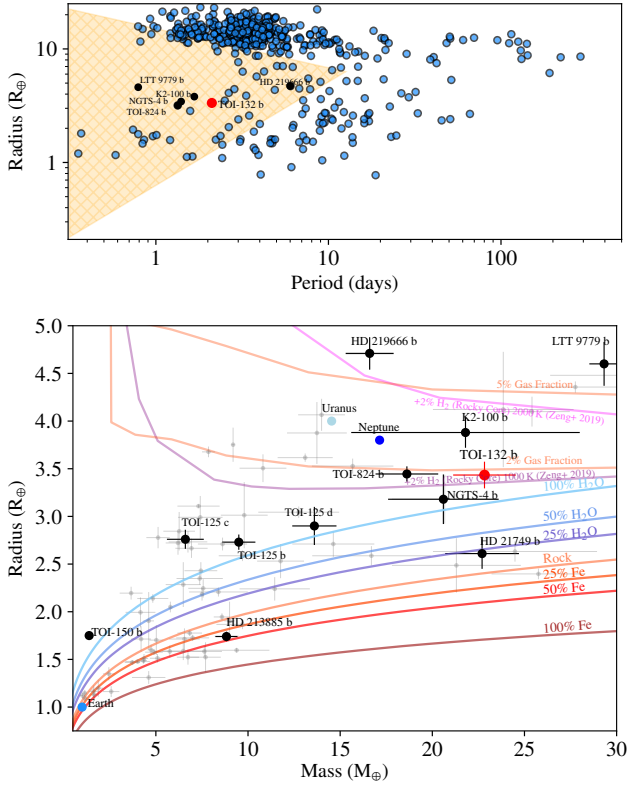


Figure 10. *Top:* Period-radius diagram for planets whose radius has been measured with a precision better than 5%. We have included recent *TESS* discoveries (Burt et al. 2019, Nielsen et al. 2019, private communication). The shaded area indicates the Neptune-desert where the edges are defined by Mazeh et al. (2016). TOI-132 b is highlighted with a red circle, near the edge of the desert. *Bottom:* Mass-radius diagram for planets whose mass and radius have been measured with a precision better than 25% (gray circles) in the range $R_p < 5R_\oplus$ and $M_p < 30M_\oplus$, retrieved from the transiting planets catalog *TEPCat* (available at <https://www.astro.keele.ac.uk/jkt/tepcat/>, Southworth 2011). Black points show recent discoveries from *TESS*. TOI-132 b is shown with a red circle. Solid, colored lines show models for different compositions from Zeng et al. (2016) ranging from 100% iron core planet to 100% H_2O planet. Also two-layer models from Zeng et al. (2019) are shown for 2% H_2 envelopes at different temperatures (magenta, purple). Extended models from (Lopez & Fortney 2014) are shown for 95% and 98% core mass fraction, 6.2 Gyr (orange).

K2-100 b, and at some point given the strong stellar irradiation on TOI-132 b could have caused atmospheric loss we see in the present.

While TOI-132 b is not as extreme in some respects as the recently discovered, first ultra hot Neptune LTT 9779 b (Jenkins et al. 2019), it is placed right at the edge of the Neptune desert. The survival of the planet’s atmosphere can likely be understood based on its large core mass, and also the incompatibility with being composed of either 100% rock or water. This would imply that, at the present time, TOI-132 b could maintain some significant gaseous atmosphere. We employed a 1-D thermal evolution model (Lopez & Fortney 2014), and for an Earth-like rocky core we find a best-fit

current day atmospheric mass fraction of $4.3^{+1.2}_{-2.3}\%$ gas, which can be retained with an initial envelope fraction of $\sim 9\%$ at 10 Myr.

With the *Gaia* parameters from Table 1, we calculated the star’s Galactic space motion. We used the IDL routine `calc_uv`, based upon Johnson & Soderblom (1987) and the local standard of rest from Coşkunoglu et al. (2011), we obtained $(U, V, W) = (18.4 \pm 0.2, -32.6 \pm 0.4, 16.5 \pm 0.4) \text{ km s}^{-1}$. Per the methodology of Reddy et al. (2006), this corresponds to a 98% probability that TOI-132 belongs to the Galactic thin disk, which is consistent with the relatively high $[\text{Fe}/\text{H}]$ we measured for the star.

The relatively high metallicity of the host star can also help to explain the large core mass fraction of the planet. Such metal-rich disks can quickly build up high-mass cores that can accumulate large fractions of gas before the disk is dispersed on timescales of $\sim 5\text{--}10$ Myrs (Baraffe et al. 2010; Mulders 2018). Indeed, we may expect more cores to have been formed in this process, possibly influencing the migration history of TOI-132 b, and therefore future precision radial-velocity measurements should be sought to search for the presence of a more rich planetary system.

In this paper, we have presented the *TESS* discovery of a Neptune-sized planet transiting the G-type star TOI-132 on the edge of the Neptune desert. Confirmation of this candidate comes from high precision HARPS spectroscopic observations that fully constrain the orbital and physical parameters of TOI-132 b. Additional ground-based photometry and speckle images provide evidence of the planetary nature of TOI-132 b. Structure models suggest that the planet can have a rocky core, retaining an atmospheric mass fraction of $4.3^{+1.2}_{-2.3}\%$. TOI-132 b stands as a *TESS* Level 1 Science Requirement candidate, which aims to precisely measure the masses for 50 transiting planets smaller than $4R_\oplus$. Therefore, future follow-up observations will allow the search for additional planets in the TOI-132 system, and also will help to constrain low-mass planet formation and evolution models, key to understanding the Neptune desert.

ACKNOWLEDGEMENTS

MRD acknowledges support of CONICYT-PFCHA/Doctorado Nacional-21140646 and Proyecto Basal AFB-170002. JSJ is supported by FONDECYT grant 1161218 and partial support from CATA-Basal (PB06, Conicyt). ZMB acknowledges funds from CONICYT-FONDECYT/Chile Postdoctorado 3180405. JIV acknowledges support of CONICYT-PFCHA/Doctorado Nacional-21191829, Chile. M.E. acknowledges the support of the DFG priority program SPP 1992 “Exploring the Diversity of Extrasolar Planets” (HA 3279/12-1). KWFL, SzCs acknowledge support by DFG grant RA 714/14-1 within the DFG Schwerpunkt SPP 1992, “Exploring the Diversity of Extrasolar Planets”. Funding for the *TESS* mission is provided by NASA’s Science Mission directorate. NN acknowledges support by JSPS KAKENHI Grant Numbers JP18H01265 and JP18H05439, and JST PRESTO Grant Number JPMJPR1775. AS acknowledges financial support from the French Programme National de Planétologie (PNP, INSU). We acknowledge the use

of *TESS* Alert data, from pipelines at the *TESS* Science Office and at the *TESS* Science Processing Operations Center. Resources supporting this work were provided by the NASA High-End Computing (HEC) Program through the NASA Advanced Supercomputing (NAS) Division at Ames Research Center for the production of the SPOC data products. This research has made use of the Exoplanet Follow-up Observation Program website, which is operated by the California Institute of Technology, under contract with the National Aeronautics and Space Administration under the Exoplanet Exploration Program. This work makes use of observations from the LCO network.

REFERENCES

- Anglada-Escudé G., et al., 2012, *ApJ*, **751**, L16
- Baraffe I., Chabrier G., Barman T., 2010, *Reports on Progress in Physics*, **73**, 016901
- Baranne A., et al., 1996, *A&AS*, **119**, 373
- Barragán O., Gandolfi D., Antoniciello G., 2019a, *MNRAS*, **482**, 1017
- Barragán O., et al., 2019b, *MNRAS*, **490**, 698
- Batalha N. M., et al., 2013, *ApJS*, **204**, 24
- Beaugé C., Nesvorný D., 2013, *The Astrophysical Journal*, **763**, 12
- Benítez-Llambay P., Masset F., Beaugé C., 2011, *Astronomy and Astrophysics*, **528**, A2
- Borucki W. J., 2010, in APS April Meeting Abstracts. p. V1.002
- Bouchy F., Pepe F., Queloz D., 2001, *A&A*, **374**, 733
- Brahm R., et al., 2019, *AJ*, **158**, 45
- Brown T. M., et al., 2013, *Publications of the Astronomical Society of the Pacific*, **125**, 1031
- Chen H., Rogers L. A., 2016, *ApJ*, **831**, 180
- Coşkunoglu B., et al., 2011, *MNRAS*, **412**, 1237
- Collins K. A., Kielkopf J. F., Stassun K. G., Hessman F. V., 2017, *AJ*, **153**, 77
- Díaz M. R., et al., 2018, *AJ*, **155**, 126
- Eastman J., 2017, EXOFASTv2: Generalized publication-quality exoplanet modeling code (ascl:1710.003)
- Eastman J., Gaudi B. S., Agol E., 2013, *PASP*, **125**, 83
- Espinoza N., 2018, Efficient Joint Sampling of Impact Parameters and Transit Depths in Transiting Exoplanet Light Curves ([arXiv:1811.04859](https://arxiv.org/abs/1811.04859))
- Espinoza N., et al., 2016, *The Astronomical Journal*, **152**, 108
- Espinoza N., et al., 2019a, arXiv e-prints, [p. arXiv:1903.07694](https://arxiv.org/abs/1903.07694)
- Espinoza N., Kossakowski D., Brahm R., 2019b, *MNRAS*, **490**, 2262
- Esposito M., et al., 2019, *A&A*, **623**, A165
- Fridlund M., et al., 2017, *A&A*, **604**, A16
- Fulton B. J., et al., 2017, *AJ*, **154**, 109
- Fulton B. J., Petigura E. A., Blunt S., Sinukoff E., 2018, *PASP*, **130**, 044504
- Gandolfi D., et al., 2019, *ApJ*, **876**, L24
- Helled R., Lozovsky M., Zucker S., 2016, *Monthly Notices of the Royal Astronomical Society*, **455**, L96
- Huang C. X., et al., 2018, *ApJ*, **868**, L39
- Jenkins J. M., 2002, *ApJ*, **575**, 493
- Jenkins J. M., 2017, Technical report, Kepler Data Processing Handbook: Overview of the Science Operations Center
- Jenkins J. M., et al., 2010, in Proc. SPIE. p. 77400D, [doi:10.1117/12.856764](https://doi.org/10.1117/12.856764)
- Jenkins J. M., et al., 2016, in Software and Cyberinfrastructure for Astronomy IV. p. 99133E, [doi:10.1117/12.2233418](https://doi.org/10.1117/12.2233418)
- Jensen E., 2013, Tapir: A web interface for transit/eclipse observability, Astrophysics Source Code Library (ascl:1306.007)
- Jin S., Mordasini C., Parmentier V., van Boekel R., Henning T., Ji J., 2014, *ApJ*, **795**, 65
- Johnson D. R. H., Soderblom D. R., 1987, *AJ*, **93**, 864
- Kipping D. M., 2013, *MNRAS*, **435**, 2152
- Kossakowski D., et al., 2019, arXiv e-prints, [p. arXiv:1906.09866](https://arxiv.org/abs/1906.09866)
- Kreidberg L., 2015, *PASP*, **127**, 1161
- Li J., Tenenbaum P., Twicken J. D., Burke C. J., Jenkins J. M., Quintana E. V., Rowe J. F., Seader S. E., 2019, *PASP*, **131**, 024506
- Lopez E. D., Fortney J. J., 2013, *ApJ*, **776**, 2
- Lopez E. D., Fortney J. J., 2014, *The Astrophysical Journal*, **792**, 1
- Lovis C., et al., 2011, arXiv e-prints, [p. arXiv:1107.5325](https://arxiv.org/abs/1107.5325)
- Lundkvist M. S., et al., 2016, *Nature Communications*, **7**, 11201
- Luque R., et al., 2019, *A&A*, **623**, A114
- Mann A. W., et al., 2017, *AJ*, **153**, 64
- Marcy G. W., et al., 2014, *ApJS*, **210**, 20
- Mayo A. W., et al., 2019, *AJ*, **158**, 165
- Mazeh T., Holzer T., Faigler S., 2016, *Astronomy and Astrophysics*, **589**, A75
- McCully C., et al., 2018, LCOGT/banzai: Initial Release, [doi:10.5281/zenodo.1257560](https://doi.org/10.5281/zenodo.1257560), <https://doi.org/10.5281/zenodo.1257560>
- Meschiari S., Wolf A. S., Rivera E., Laughlin G., Vogt S., Butler P., 2009, *PASP*, **121**, 1016
- Mulders G. D., 2018, Planet Populations as a Function of Stellar Properties. p. 153, [doi:10.1007/978-3-319-55333-7_153](https://doi.org/10.1007/978-3-319-55333-7_153)
- Owen J. E., Lai D., 2018, *Monthly Notices of the Royal Astronomical Society*, **479**, 5012
- Owen J. E., Wu Y., 2013, *ApJ*, **775**, 105
- Palle E., et al., 2019, *A&A*, **623**, A41
- Pepe F., et al., 2002, *The Messenger*, **110**, 9
- Persson C. M., et al., 2018, *A&A*, **618**, A33
- Persson C. M., et al., 2019, *A&A*, **628**, A64
- Petigura E. A., Howard A. W., Marcy G. W., 2013, *Proceedings of the National Academy of Science*, **110**, 19273
- Piskunov N., Valenti J. A., 2017, *A&A*, **597**, A16
- Pojmanski G., 1997, *Acta Astron.*, **47**, 467
- Queloz D., et al., 2001, *A&A*, **379**, 279
- Reddy B. E., Lambert D. L., Allende Prieto C., 2006, *MNRAS*, **367**, 1329
- Ricker G. R., et al., 2015, *Journal of Astronomical Telescopes, Instruments, and Systems*, **1**, 014003
- Santerne A., et al., 2015, *MNRAS*, **451**, 2337
- Schlegel D. J., Finkbeiner D. P., Davis M., 1998, *ApJ*, **500**, 525
- Smith J. C., et al., 2012, *PASP*, **124**, 1000
- Soto M. G., Jenkins J. S., 2018, *A&A*, **615**, A76
- Southworth J., 2011, *MNRAS*, **417**, 2166
- Speagle J. S., 2019, arXiv e-prints, [p. arXiv:1904.02180](https://arxiv.org/abs/1904.02180)
- Speagle J. S., Barbary K., 2018, dynesty: Dynamic Nested Sampling package, Astrophysics Source Code Library (ascl:1809.013)
- Stassun K. G., Torres G., 2016, *AJ*, **152**, 180
- Stassun K. G., Torres G., 2018, *ApJ*, **862**, 61
- Stassun K. G., Collins K. A., Gaudi B. S., 2017, *AJ*, **153**, 136
- Stassun K. G., Corsaro E., Pepper J. A., Gaudi B. S., 2018a, *AJ*, **155**, 22
- Stassun K. G., et al., 2018b, *AJ*, **156**, 102
- Stumpe M. C., Smith J. C., Catanzarite J. H., Van Cleve J. E., Jenkins J. M., Twicken J. D., Girouard F. R., 2014, *PASP*, **126**, 100
- Szabó G. M., Kiss L. L., 2011, *The Astrophysical Journal*, **727**, L44
- Tokovinin A., Mason B. D., Hartkopf W. I., Mendez R. A., Horch E. P., 2018, *AJ*, **155**, 235
- Torres G., Andersen J., Giménez A., 2010, *A&ARv*, **18**, 67
- Twicken J. D., et al., 2018, in American Astronomical Society Meeting Abstracts #232. p. 120.04

- Valenti J. A., Piskunov N., 1996a, *A&AS*, **118**, 595
- Valenti J. A., Piskunov N., 1996b, *A&AS*, **118**, 595
- Van Eylen V., Agentoft C., Lundkvist M. S., Kjeldsen H., Owen J. E., Fulton B. J., Petigura E., Snellen I., 2018, *MNRAS*, **479**, 4786
- West R. G., et al., 2019, *Monthly Notices of the Royal Astronomical Society*, **486**, 5094
- Wheatley P. J., et al., 2018, *Monthly Notices of the Royal Astronomical Society*, **475**, 4476
- Yee S. W., Petigura E. A., von Braun K., 2017, *ApJ*, **836**, 77
- Zechmeister M., Kürster M., 2009, *A&A*, **496**, 577
- Zechmeister M., et al., 2013, *A&A*, **552**, A78
- Zeng L., Sasselov D. D., Jacobsen S. B., 2016, *ApJ*, **819**, 127
- Zeng L., et al., 2019, *Proceedings of the National Academy of Sciences*, **116**, 9723
- ¹Departamento de Astronomía, Universidad de Chile, Camino El Observatorio 1515, Las Condes, Santiago, Chile.
- ²Dipartimento di Fisica, Università degli Studi di Torino, via Pietro Giuria 1, I-10125, Torino, Italy.
- ³NASA Goddard Space Flight Center, Greenbelt, MD, USA.
- ⁴School of Physics and Astronomy, Queen Mary University of London, G.O. Jones Building, 327 Mile End Road London, E1 4NS, UK.
- ⁵Vanderbilt University, Department of Physics & Astronomy, 6301 Stevenson Center Ln., Nashville, TN 37235, USA.
- ⁶Fisk University, Department of Physics, 1000 17th Ave. N., Nashville, TN 37208, USA.
- ⁷Center for Astrophysics | Harvard & Smithsonian, 60 Garden Street, Cambridge, MA 02138, USA.
- ⁸Dunlap Institute for Astronomy and Astrophysics, University of Toronto, Ontario M5S 3H4, Canada.
- ⁹Department of Space, Earth and Environment, Chalmers University of Technology, Onsala Space Observatory, SE-439 92 Onsala, Sweden.
- ¹⁰Leiden Observatory, University of Leiden, PO Box 9513, 2300 RA, Leiden, The Netherlands.
- ¹¹Dept. of Physics & Astronomy, Swarthmore College, Swarthmore PA 19081, USA.
- ¹²Instituto de Astrofísica de Canarias, Vía Láctea s/n, E-38205 La Laguna, Tenerife, Spain.
- ¹³Departamento de Astrofísica, Universidad de La Laguna, Spain.
- ¹⁴Aix Marseille Univ, CNRS, CNES, LAM, Marseille, France.
- ¹⁵University of Warwick, Department of Physics, Gibbet Hill Road, Coventry, CV4 7AL, UK.
- ¹⁶Thüringer Landessternwarte Tautenburg, Sternwarte 5, 07778, Tautenburg, Germany.
- ¹⁷Las Cumbres Observatory, 6740 Cortona Dr., Ste. 102, Goleta, CA 93117, USA.
- ¹⁸Center for Astronomy and Astrophysics, Technical University Berlin, Hardenbergstr. 36, 10623 Berlin, Germany.
- ¹⁹Department of Astronomy, University of Tokyo, 7-3-1 Hongo, Bunkyo-ku, Tokyo 113-0033, Japan.
- ²⁰Mullard Space Science Laboratory, University College London, Holmbury St Mary, Dorking, Surrey RH5 6NT, UK.
- ²¹Department of Astrophysical Sciences, Princeton University, 4 Ivy Lane, Princeton, NJ 08540, USA.
- ²²Astrobiology Center, 2-21-1 Osawa, Mitaka, Tokyo 181-8588, Japan.
- ²³JST, PRESTO, 2-21-1 Osawa, Mitaka, Tokyo 181-8588, Japan.
- ²⁴National Astronomical Observatory of Japan, 2-21-1 Osawa, Mitaka, Tokyo 181-8588, Japan.
- ²⁵Cerro Tololo Inter-American Observatory, Casilla 603, La Serena, Chile.
- ²⁶George Mason University, 4400 University Drive, Fairfax, VA, 22030, USA.
- ²⁷German Aerospace Center, Institute of Planetary Research, 12489 Berlin, Rutherfordstrasse 2, Germany.
- ²⁸MIT Kavli Institute for Astrophysics and Space Research, Massachusetts Institute of Technology, 77 Massachusetts Avenue, 37-241, Cambridge MA 02139, USA.
- ²⁹Physics Department and Tsinghua Centre for Astrophysics, Tsinghua University, Beijing 100084, China.
- ³⁰Department of Earth, Atmospheric and Planetary Sciences, Massachusetts Institute of Technology, Cambridge, MA 02139, USA.
- ³¹NASA Ames Research Center, Moffet Field, CA 94035, USA.
- ³²Department of Physics and Astronomy, University of North Carolina at Chapel Hill, Chapel Hill, NC 27599-3255, USA.
- ³³SETI Institute, 189 Bernardo Ave, Suite 200, Mountain View, CA 94043, USA.
- ³⁴Department of Aeronautics and Astronautics, MIT, 77 Massachusetts Avenue, Cambridge, MA 02139, USA.
- ³⁵Perth Exoplanet Survey Telescope, Perth, Western Australia.
- ³⁶Department of Astronomy, The University of Texas at Austin, 2515 Speedway, Stop C1400 Austin, Texas 78712-1205, USA.